8

Determination of Volume Transport Stream Function

The P-vector inverse method has been successfully used to invert the absolute velocity from hydrographic data for the extra-equatorial hemispheres, but not for the equatorial region since it is based on the geostrophic balance. A smooth interpolation scheme across the equator is described in this chapter to bring together the two already known solutions (P-vectors) for the extra-equatorial hemispheres, using the volume transport stream function Ψ.

8.1 Vertically Integrated Velocity

Starting from the basic (1.1a)–(1.1d), compute the depth-integrated (total) horizontal velocity

$$(\hat{U}, \hat{V}) = \int_{-H}^{0} (\hat{u}, \hat{v}) \mathrm{d}z, \tag{8.1}$$

and geostrophic velocity,

$$(U, V) = \int_{-H}^{0} (u, v) \mathrm{d}z \tag{8.2}$$

where $z = -H(x, y)$ represents the ocean bottom, and $z = 0$ refers to the ocean surface. Depth-integration of (1.1a) and (1.1b) from the ocean bottom to the ocean surface leads to

$$\begin{aligned} -f(\hat{V} - V) = A_z \left.\frac{\partial \hat{u}}{\partial z}\right|_{z=\eta} - A_z \left.\frac{\partial \hat{u}}{\partial z}\right|_{z=-H} \\ + A_h \nabla_2^2 \hat{U} - 2A_h \nabla_2 u_{-H} \cdot \nabla_2 H - A_h u_{-H} \nabla_2^2 H, \end{aligned} \tag{8.3}$$

$$f(\hat{U}-U) = A_z \left.\frac{\partial \hat{v}}{\partial z}\right|_{z=\eta} - A_z \left.\frac{\partial \hat{v}}{\partial z}\right|_{z=-H}$$

$$+A_h\nabla_2^2\hat{V} - 2A_h\nabla_2 v_{-H}\cdot\nabla_2 H - A_h v_{-H}\nabla_2^2 H, \qquad (8.4)$$

where (u_{-H}, v_{-H}) are velocity components at the ocean bottom. The turbulent momentum flux at the ocean surface is calculated by

$$A_z\left(\frac{\partial \hat{u}}{\partial z}, \frac{\partial \hat{v}}{\partial z}\right)\bigg|_{z=\eta} = \frac{(\tau_x, \tau_y)}{\rho_0}, \qquad (8.5)$$

where (τ_x, τ_y) are the surface wind stress components. The turbulent momentum flux at the ocean bottom is parameterized by

$$A_z\left(\frac{\partial \hat{u}}{\partial z}, \frac{\partial \hat{v}}{\partial z}\right)\bigg|_{z=-H} = C_{\mathrm{D}}\sqrt{u_{-H}^2 + v_{-H}^2}(u_{-H}, v_{-H}), \qquad (8.6)$$

where $C_{\mathrm{D}} = 0.0025$ (Blumberg and Mellor 1987) is the drag coefficient. Substituting the thermal wind relations (1.4) and (1.5) into (8.2) yields

$$(U, V) = (U_{\mathrm{den}} + Hu_{-H}, V_{\mathrm{den}} + Hv_{-H}), \qquad (8.7)$$

where

$$(U_{\mathrm{den}}, V_{\mathrm{den}}) = \frac{g}{f\rho_0}\left(\int_{-H}^{0}\int_{-H}^{z}\frac{\partial \rho}{\partial y}\mathrm{d}z'\,\mathrm{d}z, -\int_{-H}^{0}\int_{-H}^{z}\frac{\partial \rho}{\partial x}\mathrm{d}z'\,\mathrm{d}z\right) \qquad (8.8)$$

is the density driven transport. Rearrange (8.3) and (8.4) into

$$A_h\nabla^2\hat{U} + f\hat{V} = fV_{\mathrm{den}} + fV_{\mathrm{b}} - \frac{\tau_x}{\rho_0} + A_h Q_1, \qquad (8.9)$$

$$-A_h\nabla^2\hat{V} + f\hat{U} = fU_{\mathrm{den}} + fU_{\mathrm{b}} + \frac{\tau_y}{\rho_0} - A_h Q_2, \qquad (8.10)$$

where

$$Q_1 \equiv (2\nabla u_{-H}\cdot\nabla H + u_{-H}\nabla^2 H), \quad Q_2 \equiv (2\nabla v_{-H}\cdot\nabla H + v_{-H}\nabla^2 H),$$

and

$$U_{\mathrm{b}} = \left(H - \frac{C_{\mathrm{D}}}{f}\sqrt{u_{-H}^2 + v_{-H}^2}\right)u_{-H}, \quad V_{\mathrm{b}} = \left(H + \frac{C_{\mathrm{D}}}{f}\sqrt{u_{-H}^2 + v_{-H}^2}\right)v_{-H}, \qquad (8.11)$$

are the transport due to the bottom currents, or in simple terms, it is called the bottom transport. With the known bottom velocity vector (u_{-H}, v_{-H}), the depth-integrated velocity (U, V) can be determined from the wind, density, and topographic data.

For the extra-equatorial regions, the horizontal diffusion can be neglected (see Sect. 1.1.2). Equations (8.10) and (8.9) become

$$U^* = U_{\rm den} + U_{\rm b} + \frac{\tau_y}{f\rho_0}, \tag{8.12}$$

$$V^* = V_{\rm den} + V_{\rm b} - \frac{\tau_x}{f\rho_0}. \tag{8.13}$$

With the known (u_{-H}, v_{-H}), the depth-integrated flow (U^*, V^*) may be directly calculated using (8.12) and (8.13). However, the computed (U^*, V^*) field using (8.12) and (8.13) is quite noisy and cannot be the final product. Thus, the superscript "*" is used to represent the interim depth-integrated velocity calculated using (8.12) and (8.13).

8.2 Volume Transport Stream Function

Integration of the continuity (1.1d) with respect to z from the bottom to the surface yields,

$$\frac{\partial \hat{U}}{\partial x} + u_{-H}\frac{\partial H}{\partial x} + \frac{\partial \hat{V}}{\partial y} + v_{-H}\frac{\partial H}{\partial y} - w_{-H} = 0. \tag{8.14}$$

The water follows the bottom topography,

$$w_{-H} = u_{-H}\frac{\partial H}{\partial x} + v_{-H}\frac{\partial H}{\partial y}. \tag{8.15}$$

Equation (8.14) becomes

$$\frac{\partial \hat{U}}{\partial x} + \frac{\partial \hat{V}}{\partial y} = 0, \tag{8.16}$$

which leads to the definition of the volume transport stream function (Ψ),

$$\hat{U} = -\frac{\partial \Psi}{\partial y}, \quad \hat{V} = \frac{\partial \Psi}{\partial x}. \tag{8.17}$$

Subtracting differentiation of (8.10) with respect to y from the differentiation of (8.9) with respect to x yields

$$\nabla^2 \Psi = \Pi, \tag{8.18}$$

where

$$\Pi \equiv \frac{1}{f}\left[\frac{\partial (fV_{\rm den})}{\partial x} - \frac{\partial (fU_{\rm den})}{\partial y}\right] + \frac{1}{f}\left[\frac{\partial (fV_{\rm b})}{\partial x} - \frac{\partial (fU_{\rm b})}{\partial y}\right]$$
$$-\frac{1}{f}\left[\frac{\partial}{\partial x}\left(\frac{\tau_x}{\rho_0}\right) + \frac{\partial}{\partial x}\left(\frac{\tau_y}{\rho_0}\right)\right] + \frac{A_h}{f}\left(\frac{\partial Q_1}{\partial x} + \frac{\partial Q_2}{\partial y}\right), \tag{8.19}$$

is the volume transport vorticity. Equation (8.18) is called the Poisson Ψ-equation.

8.3 Volume Transport Vorticity

8.3.1 Extra-Equatorial Region

For extra-equatorial region, the horizontal diffusion can be neglected, (8.19) becomes

$$\Pi \equiv \frac{1}{f}\left[\frac{\partial(fV_{\rm den})}{\partial x} - \frac{\partial(fU_{\rm den})}{\partial y}\right] + \frac{1}{f}\left[\frac{\partial(fV_{\rm b})}{\partial x} - \frac{\partial(fU_{\rm b})}{\partial y}\right]$$

$$-\frac{1}{f}\left[\frac{\partial}{\partial x}\left(\frac{\tau_x}{\rho_0}\right) + \frac{\partial}{\partial x}\left(\frac{\tau_y}{\rho_0}\right)\right]. \tag{8.20}$$

The volume transport vorticity Π for the extra-equatorial regions can be computed from observational data using (8.21). This is because $(U_{\rm den}, V_{\rm den})$ depend on ρ only; (τ_x, τ_y) are wind stress components; and (U_b, V_b) are determined by the bottom current velocity (u_{-H}, v_{-H}). The P-vector inverse method described in Chaps. 5 and 6 is used to determine (u_{-H}, v_{-H}) from hydrographic data.

The calculated volume transport vorticity Π is quite noisy even from climatological data (Fig. 8.1). In this case, the climatological hydrographic data (e.g., GDEM or WOA) are used to compute $(U_{\rm den}, V_{\rm den})$ [see (8.8)]. The climatological surface wind stress (τ_x, τ_y) data are obtained from climatological wind data such as the Comprehensive Ocean-Atmosphere Data Set (da Silva et al. 1994). The bottom topography is obtained from the Navy's Digital Bathymetry Data Base 5-minute (DBDB5).

8.3.2 Equatorial Region (between 8°S and 8°N)

In the equatorial region, the Coriolis parameter f is small. The horizontal gradient of the Reynolds stress cannot be neglected and (8.21) cannot be used to determine the function Π. Summation of the differentiation of (8.9) with respect to y and the differentiation of (8.10) with respect to x and the use of (8.18) yield the volume transport vorticity equation,

$$\nabla^2\Pi = \frac{\beta}{A_h}(\hat{V} - V_{\rm den} - V_{\rm b}) - \frac{1}{A_h\rho_0}\left(\frac{\partial\tau_y}{\partial x} - \frac{\partial\tau_x}{\partial y}\right) + \left(\frac{\partial Q_2}{\partial x} - \frac{\partial Q_1}{\partial y}\right). \tag{8.21}$$

For the extra-equatorial regions, $A_h \cong 0$, (8.21) becomes the Sverdrup (1947) relation

$$\beta(\hat{V} - V_{\rm den} - V_{\rm b}) = \frac{1}{\rho_0}\left(\frac{\partial\tau_y}{\partial x} - \frac{\partial\tau_x}{\partial y}\right). \tag{8.22}$$

The northern and southern boundary values of Π are computed using (8.20). The volume transport vorticity (8.21) is solved with the boundary values of Π (Fig. 8.2) and the cyclic eastern and western boundary conditions, and the Π-values in the equatorial region between 8°N and 8°S are obtained. Figure 8.3 shows annual, January, and July mean distributions of Π-values for the equatorial region (8°S–8°N). The computed Π-field is quite smooth.

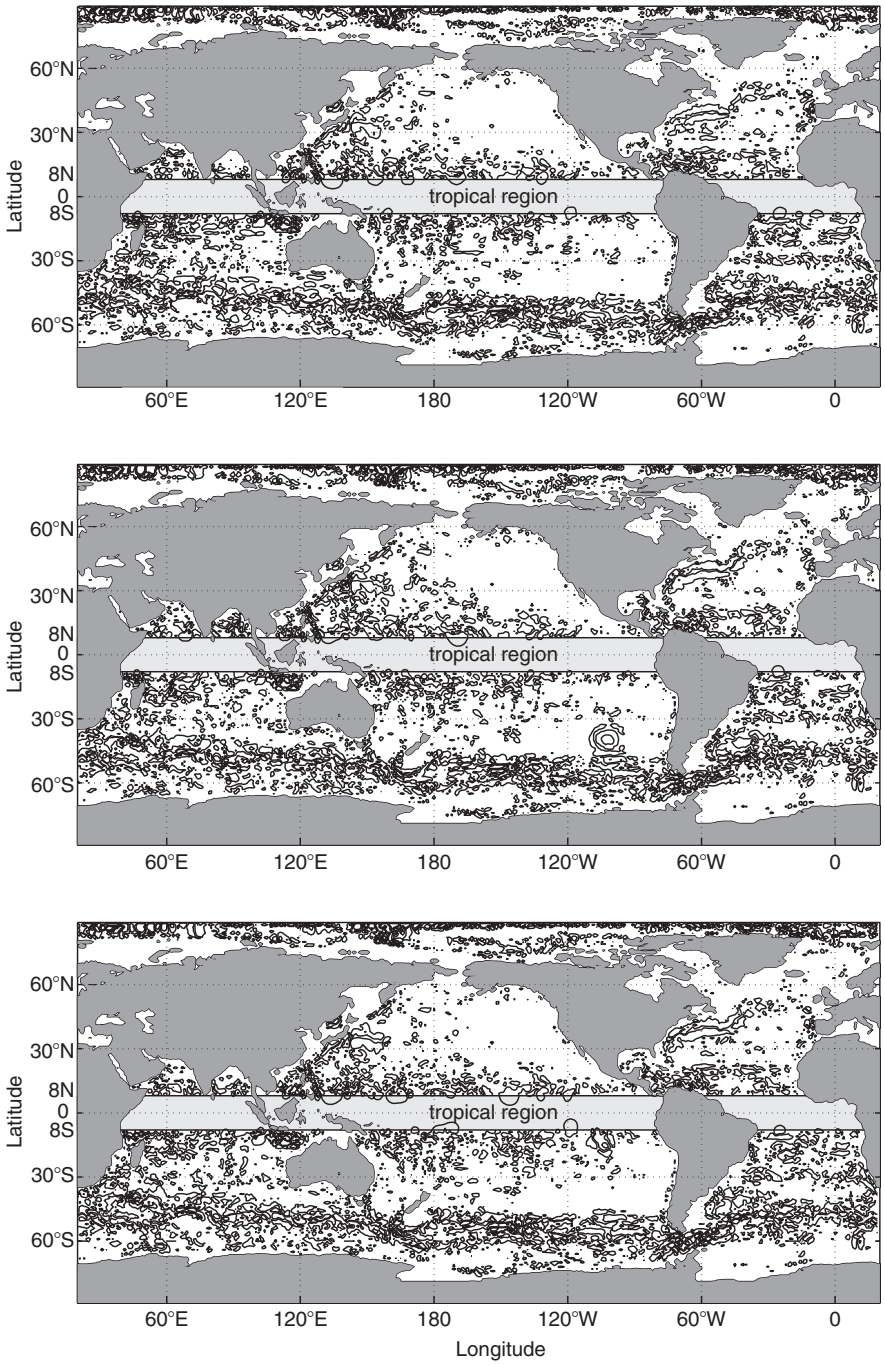

Fig. 8.1. Distributions of Π for the extra-equatorial regions (**a**) annual mean, (**b**) January, and (**c**) July (from Chu and Fan 2006, Journal of Marine Systems)

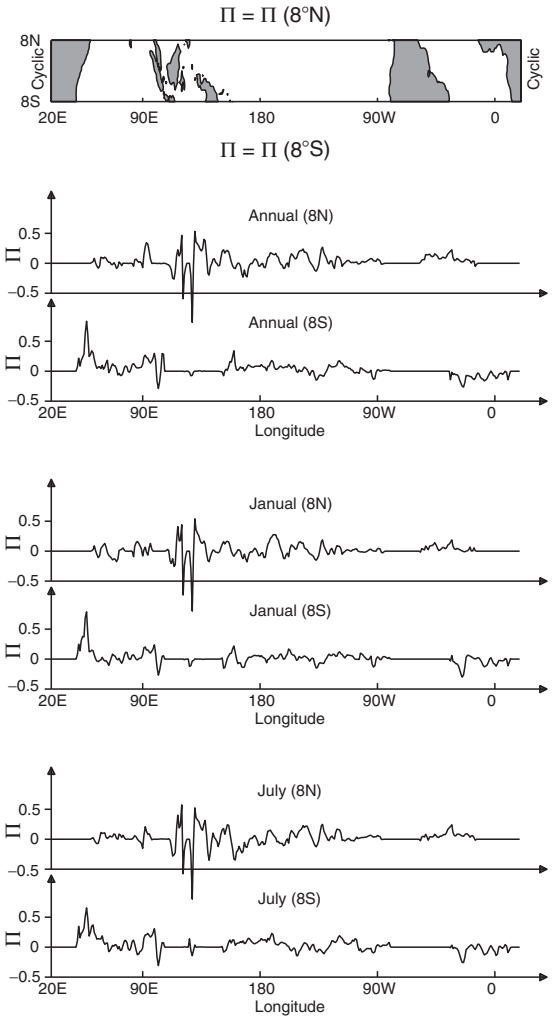

Fig. 8.2. Northern (8°N) and southern (8°S) boundary conditions of Π for the tropical regions (from Chu and Fan 2006, Journal of Marine Systems)

8.4 Boundary Conditions for Poisson Ψ-Equation

The computation described in Sect. 8.3 yields the global volume transport vorticity (Π), which is the forcing term of the Poisson Ψ-equation (8.18). In order to solve (8.18), we need boundary conditions. The flow across the Antarctic Continent does not lead to the southern boundary condition

$$\Psi = C_1, \quad \text{at the southern boundary } y = y_s \tag{8.23}$$

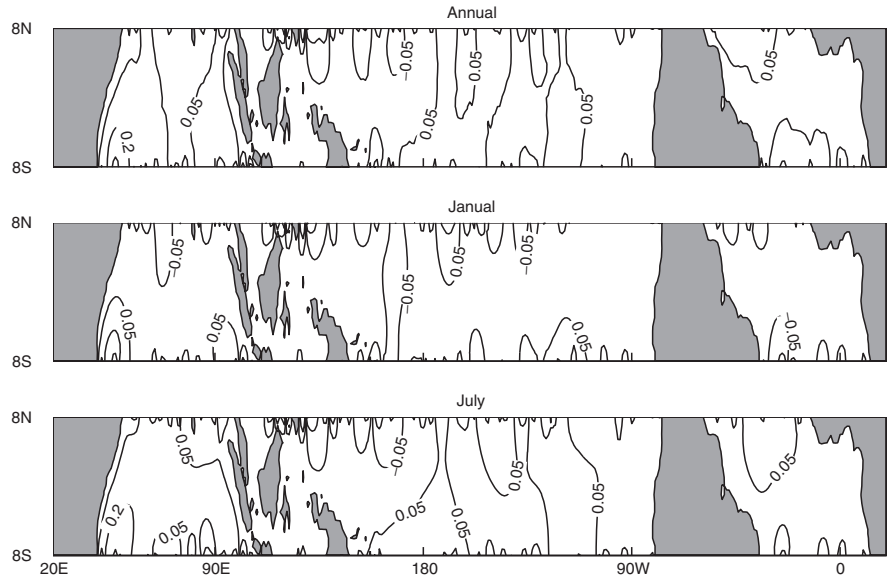

Fig. 8.3. Solutions of the volume transport vorticity (8.21) representing the distributions of Π for the equatorial regions (**a**) annual mean, (**b**) January, and (**c**) July (from Chu and Fan 2006, Journal of Marine Systems)

The horizontal convergence of the 2D flow $(\hat{U}, \hat{V})$ at the North Pole does not lead to the northern boundary condition

$$\Psi = C_2, \quad \text{at the northern boundary } y = y_\mathrm{n}, \tag{8.24}$$

where C_1 and C_2 are constants (to be determined). The cyclic boundary condition is applied to the western and the eastern boundaries (Fig. 8.4).

We integrate $\partial\Psi/\partial y = -U^*$ with respect to y along the western (or eastern) boundary from the southern boundary ($\Psi = 0$) to the northern boundary to obtain

$$\Psi|_\mathrm{west}(y) = -\int_{y_\mathrm{s}}^{y} U^*(x_\mathrm{west}, y')\mathrm{d}y'. \tag{8.25}$$

The cyclic boundary condition gives

$$\Psi|_\mathrm{east}(y) = \Psi|_\mathrm{west}(y) \tag{8.26}$$

8.5 Determination of Ψ-Values at Islands

Before solving the Poisson Ψ-equation (8.18) with the boundary conditions (8.23)–(8.26), the Ψ-values at all islands should be given. These values

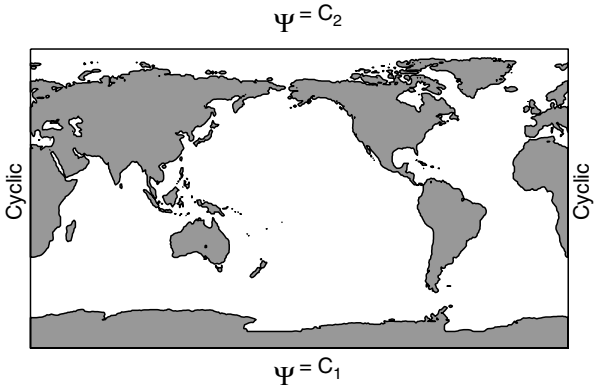

Fig. 8.4. Boundary conditions of Ψ for the global ocean (from Chu and Fan 2006, Journal of Marine Systems)

were subjectively set up in earlier studies. For example, in calculating the geostrophic transport in the Pacific Ocean, Reid (1997) set up Ψ-value to be 0 for Antarctic, 135 Sv for Australia, and 130 Sv for America. In calculating the geostrophic transport in the South Atlantic Ocean, Reid (1989) set up Ψ-value to be 0 for Antarctic, 132 Sv for Africa, and 130 Sv for America. Such a treatment subjectively prescribes 130 Sv through the Drake Passage and 132 Sv through the area between Africa and Antarctica. Godfrey (1989) used the Sverdrup model to compute Ψ-values at islands. In this section, a more general method on the basis of the Stokes circulation theorem is presented for determining Ψ-value at islands.

8.5.1 Stokes Theorem

Let the ocean basin be defined as a domain Ω and islands as $\Omega_j (j = 1, \ldots, N)$ in (x, y) space with uniform grids $(\Delta x, \Delta y)$ and assume the multiple connection with horizontal boundaries of closed solid-wall segments (i.e., islands) of $\delta\Omega_j, j = 1, \ldots, N$. The domain Ω may have open boundaries. Figure 8.5 shows a schematic illustration of such a domain with open boundary segments and islands.

In order to determine the boundary conditions for islands, McWilliams 1977 defined a simply connected fluid region between an island $(\delta\Omega_j)$ and a clockwise circuit in the fluid interior $(\delta\omega_j)$. Let C_j denote the closed area bounded by $\delta\Omega_j$ and $\delta\omega_j$, and $(\mathbf{n}, \mathbf{s})$ be the normal (positive outward) and tangential unit vectors along the boundaries of C_j.

The circulation around the boundary of C_j is calculated using the Stokes Theorem,

$$-\oint_{\delta\Omega_j} \hat{\mathbf{V}} \cdot \mathbf{s}\, \mathrm{d}l + \oint_{\delta\omega_j} \hat{\mathbf{V}} \cdot \mathbf{s}\, \mathrm{d}l = \int\int_{C_j} \mathbf{k} \cdot (\nabla \times \hat{\mathbf{V}}) \mathrm{d}x\, \mathrm{d}y \tag{8.27}$$

where l is the path along the boundary of C_j. The direction of closed integration $\oint$ is defined as anticlockwise. Substituting the volume transport stream function (8.17) into the first term in the left-hand side of (8.27) yields

$$\oint_{\delta\Omega_j} \nabla\Psi \cdot \mathbf{n}\,\mathrm{d}l = \oint_{\delta\omega_j} \hat{\mathbf{V}} \cdot \mathbf{s}\,\mathrm{d}l - \iint_{C_j} \mathbf{k} \cdot (\nabla \times \hat{\mathbf{V}})\mathrm{d}x\,\mathrm{d}y, \tag{8.28}$$

and determines the Ψ-value at Island-Ω_j.

The smaller the area of C_j, the smaller the value of the second term in the right-hand side of (8.28), i.e.,

$$\oint_{\delta\Omega_j} \nabla\Psi \cdot \mathbf{n}\,\mathrm{d}l \to \Gamma_j \quad \text{as}\, C_j \to 0, \tag{8.29}$$

where

$$\Gamma_j = \oint_{\delta\omega_j} \mathbf{V} \cdot \mathbf{s}\,\mathrm{d}l$$

Thus, selection of $\delta\omega_j$ with a minimum C_j becomes a key issue in determining the stream function, $\Psi|_{\Omega_j}$. Such a circuit $(\delta\omega_j^*)$ is called the minimum circuit along the island Ω_j (Fig. 8.5). Let (I_l, J_l) $(l = 1, \ldots, N+1)$ be the anticlockwise rotating grid points along $\delta\omega_j^*$ with $(I_{N+1}, J_{N+1}) = (I_1, J_1)$, and let the circulation along $\delta\omega_j^*$ be denoted by $\hat{\Gamma}_j$ and computed by

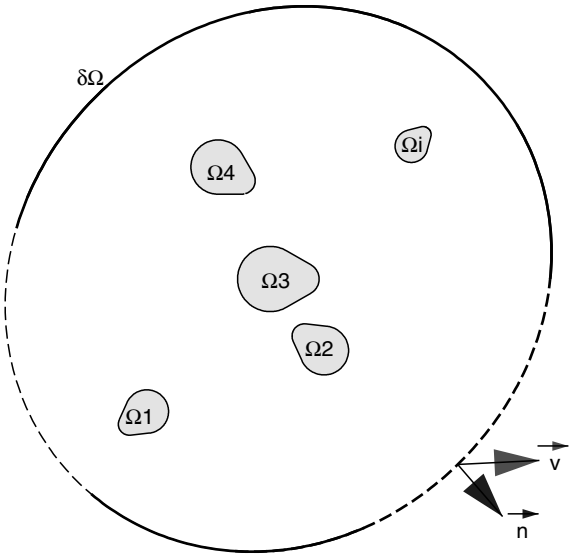

Fig. 8.5. Multiple connected domain. The *arrows* indicate the directions of integration along the line as the integral paths defined in the text (from Chu and Fan 2006, Journal of Marine Systems)

$$\hat{\Gamma}_j = \frac{1}{2}\sum_{l=1}^{N}[\hat{\mathbf{V}}(I_l,J_l)+\hat{\mathbf{V}}(I_{l+1},J_{l+1})]\cdot[\mathbf{i}(I_{l+1}-I_l)\Delta x+\mathbf{j}(J_{L+1}-J_l)\Delta y], \quad (8.30)$$

which depends solely on the island geometry and the velocity field ($\hat{\mathbf{V}}$).

8.5.2 Algebraic Equation for Ψ-Value at Island-Ω_j

The left-hand side of (8.29) is discretized by

$$\oint_{\delta\Omega_j}\nabla\Psi\cdot\mathbf{n}\,\mathrm{d}l \doteq \sum_{l=1}^{N}\frac{(I_{l+1}-I_l)\Delta x}{\Delta y}[\Psi(I_l,J_l-1)+\Psi(I_{l+1},J_{l+1}-1)$$

$$-\Psi(I_l,J_l+1)-\Psi(I_{l+1},J_{l+1}+1)]+\sum_{l=1}^{N}\frac{(J_{l+1}-J_l)\Delta y}{\Delta x}$$

$$\times[\Psi(I_l+1,J_l)+\Psi(I_{l+1}+1,J_{l+1})$$

$$-\Psi(I_l-1,J_l)-\Psi(I_{l+1}-1,J_{l+1})]. \quad (8.31)$$

Since the grid points on the island Ω_j are always on the left side of the anticlockwise circulation $\hat{\Gamma}_j$ (Fig. 8.6), half grid points of (8.31) are in the island and half in the water. Thus, (8.31) can be rewritten by

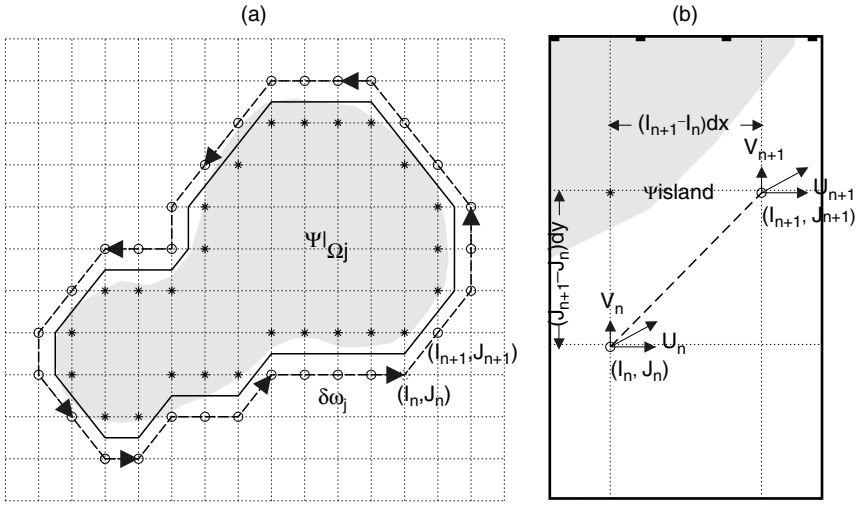

Fig. 8.6. Grid points around the island, Ω_j (from Chu and Fan 2006, Journal of Marine Systems)

$$\hat{\Gamma}_j = A\Psi|_{\Omega_j} + \Gamma_j^{(w)}, \tag{8.32}$$

where $\Gamma_j^{(\mathrm{w})}$ is the circulation in the water and

$$A = -\sum_{l=1}^{N} \left(\frac{|J_{l+1} - J_l|\Delta y}{2\Delta x} + \frac{|I_{l+1} - I_l|\Delta x}{2\Delta y} \right). \tag{8.33}$$

The volume transport stream function at Island-Ω_j is computed by

$$\Psi|_{\Omega_j} = \frac{\hat{\Gamma}_j - \Gamma_j^{(\mathrm{w})}}{A}. \tag{8.34}$$

8.5.3 Iteration Process

Equation (8.34) cannot be directly used to compute $\Psi|_{\Omega_j}$ even if the vertically integrated velocity $(\hat{U}, \hat{V})$ is given. This is because that the Ψ-values at surrounding water is still undetermined. Thus, we use an iterative process to determine $\Psi|_{\Omega_j}$ from a first guess value. Suppose all the islands Ω_j $(j = 2, \ldots, N)$ in Fig. 8.5 has to be removed, with the given boundary conditions at $\delta\Omega_1$, we solve the Poisson Ψ-equation (8.18) and obtain the solution $\Psi^*(x, y)$. The average of Ψ^* over Ω_j leads to the first guess Ψ-values at islands Ω_j $(j = 2, \ldots, \mathrm{N})$,

$$\Psi|_{\Omega_j}(0) = \int\int_{\Omega_j} \Psi^*(x, y)\mathrm{d}x\,\mathrm{d}y. \tag{8.35}$$

Let Ψ-values and the circulation $\hat{\Gamma}_j$ be given at the mth iteration such that

$$\Psi|_{\Omega_j}(m) = \frac{\Gamma_j^*(m) - \sum\limits_k B_k \Psi_k(m)}{A}, \tag{8.36}$$

where the minimum circuit circulation at the mth iteration, $\Gamma_j^*(m)$, might not be the same as $\hat{\Gamma}_j$. We update $\Psi|_{\Omega_j}$ using

$$\Psi|_{\Omega_j}(m) = \frac{\Gamma_j^*(m) - \sum\limits_k B_k \Psi_k(m)}{A}. \tag{8.37}$$

Subtracting (7.40) from (7.41) yields

$$\Psi|_{\Omega_j}(m+1) = \Psi|_{\Omega_j}(m) + \frac{\hat{\Gamma}_j - \Gamma_j^*(m)}{A}, \tag{8.38}$$

which indicates the iteration process (a) solving the Poisson Ψ-equation (8.18) with $\Psi|_{\Omega_j}(m)$ to obtain solutions and in turn to get $\Gamma_j^*(m)$, (b) replacing the Ψ-values at islands using (8.38). The iteration process (Fig. 8.7) repeats until it reaches a certain criterion

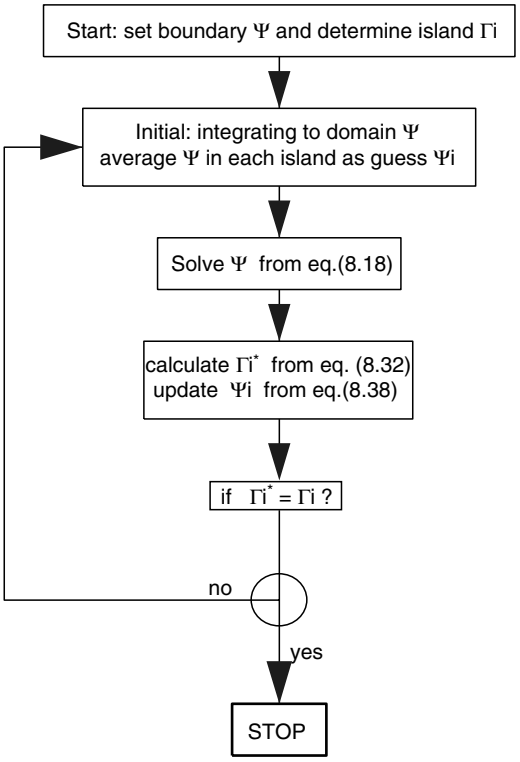

Fig. 8.7. Flow chart, showing the iteration method for determining $\Psi|_{\Omega_j}$

$$\frac{|\delta \mathbf{\Gamma}^*|}{|\hat{\mathbf{\Gamma}}|} \leq \varepsilon, \tag{8.39}$$

where

$$|\hat{\mathbf{\Gamma}}| \equiv \sqrt{\frac{1}{N}\sum_{j=1}^{N}[\hat{\Gamma}_j]^2}, \quad |\delta \mathbf{\Gamma}^*| \equiv \sqrt{\frac{1}{N}[\Gamma_j^*(m+1) - \Gamma_j^*(m)]^2}, \tag{8.40}$$

and ε is a small positive number (user input), which is set to be 10^{-6} in this study. As soon as the inequality (8.39) is satisfied, the iteration stops and the final set of $\{\Psi|_{\Omega_j},\, j = 1, 2, \ldots, \mathrm{N}\}$ become the optimal Ψ-values for islands.

8.6 Verification of Island Algorithm

8.6.1 A Channel with Two Islands

Consider a channel (length: L, width: W) with a uniform depth and two irregular shaped islands (Fig. 8.8), where a larger one (Island-1) is located in

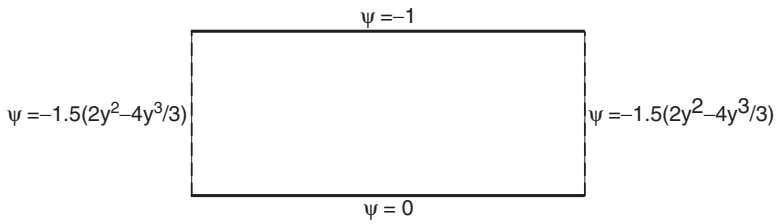

Fig. 8.8. Boundary conditions of the channel flow. Note that y is nondimensional

the middle of the channel, and a smaller one (Island-2) is located southwest of Island-1.

Let x- and y-axes be along the southern and western boundaries with the origin at the southwest corner and be nondimensionalized by W. The northern and southern boundaries of the channel are rigid, and the western and eastern boundaries are cyclic. A nondimensional mathematical model for the test consists of the Poisson equation [see (8.18)]

$$\nabla^2 \Psi = \Pi,$$

with the boundary conditions (Fig. 8.8)

$$\Psi|_{y=0} = 0, \quad \Psi|_{y=1} = -1, \quad \Psi|_{x=0} = \Psi|_{x=L/W} = -1.5\left(2y^2 - \frac{4}{3}y^3\right), \tag{8.41}$$

where the mean inflow (outflow) velocity is taken as a unit velocity. We will test if the method has the capability to determine Ψ-values at the islands for a given forcing

$$\Pi = \frac{\mathrm{d}^2\Psi(0)}{\mathrm{d}y^2} = -6(1-2y). \tag{8.42}$$

8.6.2 Twin Experiments

Twin experiments are designed to test the validity of the method and to get the "exact" Ψ data for the verification. In the first experiment (control run), we integrate the Poisson Ψ-equation (8.18) with (8.41) and with the given Ψ-values at the two islands $(\Psi_1^{(\mathrm{I})}, \Psi_2^{(\mathrm{I})})$, we obtain the solution $\Psi^{(\mathrm{ex})}(x, y)$ as the "exact" data for the evaluation. Here,

$$\Psi_1^{(\mathrm{I})} = (-1, -7/8, -3/4, -1/2, -3/8, -1/4, -1/8, 0)\Psi_2^{(\mathrm{I})} = -0.1. \tag{8.43}$$

The varying $\Psi_1^{(\mathrm{I})}$ changes the flow pattern. As $\Psi_1^{(I)} = -0.5$, the flow is almost symmetric north and south of Island-1. As $\Psi_1^{(\mathrm{I})} = 0$, the flow almost totally passes through between the north boundary and Island-1. As $\Psi_1^{(\mathrm{I})} = -1$, the flow almost totally passes through between the south boundary and Island-1 (Fig. 8.9). Also, the velocity field computed by

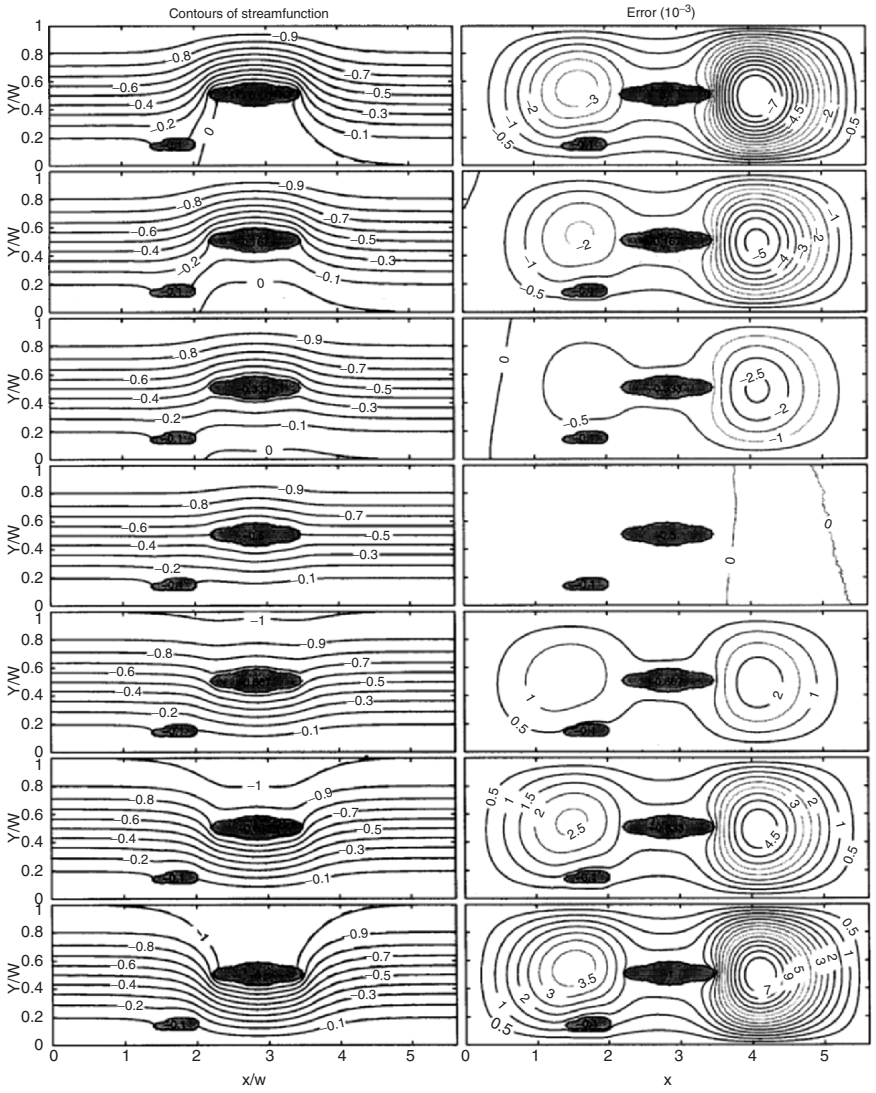

Fig. 8.9. *Left panels*: comparison between $\Psi^{(\mathrm{ex})}(x, y)$ (*solid contours*) and $\Psi(x, y)$ (*dashed contours*) for $\Psi_1^{(\mathrm{I})}$ varying from -1 to 0 (keeping Island-1 at the same location) in the control run of the twin experiments. *Right panels*: The corresponding difference, $\Psi^{(\mathrm{ex})}(x, y) - \Psi(x, y)$, for each case

$$\hat{U}^{(\mathrm{ex})} = -\frac{\partial \Psi^{(\mathrm{ex})}}{\partial y}, \quad \hat{V}^{(\mathrm{ex})} = \frac{\partial \Psi^{(\mathrm{ex})}}{\partial x}, \tag{8.44}$$

is used to compute the circulation $\hat{\Gamma}_1$ and $\hat{\Gamma}_2$ around the two islands for the second experiment (sensitivity run).

In the second experiment (sensitivity run), the Ψ-values at the two islands are unknown. We use (8.30) and (8.38) to compute the Ψ-values at the two islands and then to solve the Poisson Ψ-equation (8.18). The evaluation is achieved through the comparison of the two solutions. To test the capability of the scheme, we perform several sensitivity studies by varying the location and $\Psi_1^{(\mathrm{I})}$-value for Island-1 and keeping them the same for Island-2, i.e., $\Psi_2^{(\mathrm{I})} = -0.1$.

8.6.3 Sensitivity to $\Psi_1^{(\mathrm{I})}$-Value

Island-1 is kept as the same location and the $\Psi_1^{(\mathrm{I})}$-value is varied [see (8.43)]. The "exact" solutions $\Psi^{(\mathrm{ex})}(x, y)$ for seven different $\Psi_1^{(\mathrm{I})}$-values are the solid contours in the left panels of Fig. 8.9. The corresponding solution,$\Psi(x, y)$, for the second experiment is represented by the dashed contours (Fig. 8.9). The difference between the two experiments (control minus sensitivity run), as illustrated in the right panels of Fig. 8.9, reveals a dual cyclonic-eddy (anticyclonic-eddy) structure in the leeward side and upwind side, respectively, when the $\Psi_1^{(\mathrm{I})}$-value is larger (smaller) than -0.5. The leeward eddy (i.e., the error) is twice as strong as the upwind eddy. Its absolute values reach a maximum around 0.007 (leeward) as $\Psi_1^{(\mathrm{I})} = 0, -1$. The errors decrease (increase) with $\Psi_1^{(\mathrm{I})}$-value from 0 to -0.5 (from -0.5 to -1). When $\Psi_1^{(\mathrm{I})} = -0.5$, we have a minimum difference between the two experiments.

In the sensitivity run, using the method, the computed stream function at the two islands (Ψ_1, Ψ_2) might not be the same as $(\Psi_1^{(\mathrm{I})}, \Psi_2^{(\mathrm{I})})$, and the solution of (8.18), $\Psi(x, y)$, might not be the same as $\Psi^{(\mathrm{ex})}(x, y)$. We calculate the relative root mean square error (rrmse) between $\Psi(x, y)$ and $\Psi^{(\mathrm{ex})}(x, y)$

$$\mathrm{rrmse} = \frac{\sqrt{\sum_i \sum_j \left[\Psi^{(\mathrm{ex})}(x_i, y_j) - \Psi(x_i, y_j)\right]^2}}{\sum_i \sum_j \left[\Psi^{(\mathrm{ex})}(x_i, y_j)\right]^2}, \tag{8.45}$$

for the whole channel and the relative errors

$$E_1 = \frac{|\Psi_1^{(\mathrm{I})} - \Psi_1|}{|\Psi_1^{(\mathrm{I})}|}, \quad E_2 = \frac{|\Psi_2^{(\mathrm{I})} - \Psi_2|}{|\Psi_2^{(\mathrm{I})}|}, \tag{8.46}$$

for the two islands.

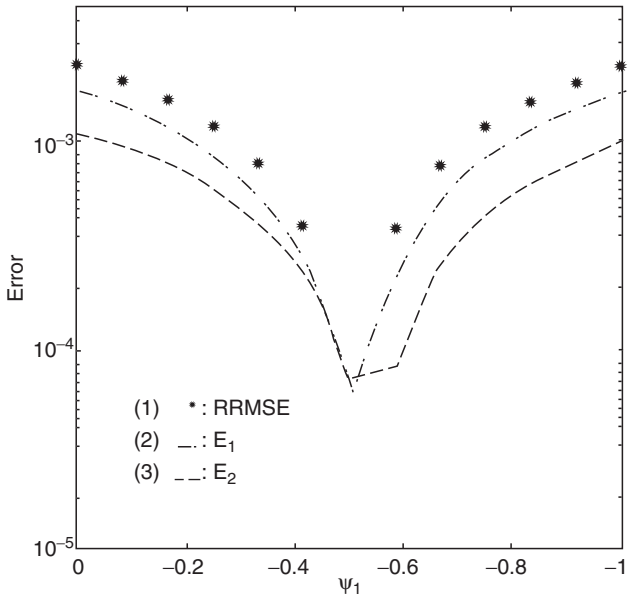

Fig. 8.10. Dependence of rrmse between $\Psi(x, y)$ and $\Psi^{(\mathrm{ex})}(x, y)$ over the whole channel (denoted by *asterisk*), and the relative errors E_1 (*dash-dotted*) and E_2 (*dashed*) on varying $\Psi_1^{(\mathrm{I})}$-values

Figure 8.10 shows the dependence of rrmse, E_1, and E_2 on $\Psi_1^{(\mathrm{I})}$. The three relative errors have the following features (a) they are lesser than 1% with the maximum relative errors,

$$\max(\mathrm{rrmse}, E_1, E_2) = (5.7, 2.0, 1.2) \times 10^{-3}; \tag{8.47}$$

(b) Minimum relative errors occur when the volume transport is relatively symmetric to Island-1 $\Psi_1^{(\mathrm{I})} = -0.5$,

$$\min(\mathrm{rrmse}, E_1, E_2) = (0.92, 0.61, 0.72) \times 10^{-4}; \tag{8.48}$$

(c) The three relative errors have a similar dependence on$\Psi_1^{(\mathrm{I})}$. They all decrease with $\Psi_1^{(\mathrm{I})}$ monotonically from the maximum errors $[(5.7, 2.0, 1.2)\times 10^{-3}]$ at $\Psi_1^{(\mathrm{I})} = -1$ (flow mostly south of Island-1) to the minimum errors $[(0.92, 0.61, 0.72)\times 10^{-4}]$ at $\Psi_1^{(\mathrm{I})} = -0.5$ – (flow relatively symmetric north and south of Island-1); and then increase with $\Psi_1^{(\mathrm{I})}$ monotonically to the maximum errors at $\Psi_1^{(\mathrm{I})} = 0$ (flow mostly north of Island-1).

8.6.4 Sensitivity to Location of Island-1

The $\Psi_1^{(\mathrm{I})}$-value (-0.5) is kept unchanged and its location (in the y-direction) is varied. The solutions $\Psi^{(\mathrm{ex})}(x, y)$ for seven different locations are shown as the

solid contours in the left panels of Fig. 8.11. The corresponding results for the second experiment are shown as the dashed contours. The difference between the two experiments (first minus second experiment), as illustrated in the right panels of Fig. 8.11, reveals an elliptic anticyclonic-eddy structure with the maximum value of 0.01 (maximum error). As Island-1 "moves" northward, the "anticyclone" weakens and splits into two smaller "anticyclones" with the leeward one being stronger than the other. When Island-1 "moves" to the center of the channel, the errors become very small. As Island-1 continues to "move" northward, a cyclonic-eddy first occurs at the leeward side of Island-1, expands toward the west, and reveals an elliptic cyclonic-eddy structure with the maximum error of 0.011.

In the second experiment, the computed stream function at the two islands (Ψ_1, Ψ_2) using this method is usually not be exactly the same as $(\Psi_1^{(\mathrm{I})}, \Psi_2^{(\mathrm{I})})$,, and the solution $\Psi(x, y)$ might not be exactly the same as $\Psi^{(\mathrm{ex})}(x, y)$. Figure 8.12 shows the dependence of rrmse, E_1, and E_2 on the location of Island-1. The three relative errors have the following features (a) they are lesser than 1% with the maximum relative errors

$$\max(\mathrm{rrmse}, E_1, E_2) = (3.7, 3.2, 1.9) \times 10^{-3}; \tag{8.49}$$

and (b) the three relative errors have a similar dependence on the location of Island-1. They all decrease with northward "displacing" Island-1 monotonically from the maximum errors [(3.7, 3.2, 1.9)] when Island-1 is located near the southern boundary (first on the left panels) to the minimum errors [(0.92, 0.61, 0.72) $\times 10^{-4}$] when Island-1 is located near the middle of the channel; and then increase with northward "displacing" Island-1 monotonically to the maximum errors $[(6.7, 3.2, 2.0) \times 10^{-3}]$ when Island-1 is located near the northern boundary.

8.6.5 Sensitivity to Noise

In reality, the velocity data contain errors. In order to test if the noisy data destroy the solution, or in other words, to test the model capability in handling the noisy data, we use a random number generator to produce a white noise $(U_{\mathrm{noise}}, V_{\mathrm{noise}})$ with different noise levels (0.00417–0.05) for each grid pointing independently and adding it to the "exact" velocity,

$$\tilde{U} = \hat{U}^{(\mathrm{ex})} + U_{\mathrm{noise}}, \quad \tilde{V} = \hat{V}^{(\mathrm{ex})} + V_{\mathrm{noise}}, \tag{8.50}$$

which is used to calculate $(\hat{\Gamma}_1, \hat{\Gamma}_2)$ around the two islands for the second experiment.

The "exact" solution $\Psi^{(\mathrm{ex})}(x, y)$ is obtained for

$$\Psi_1^{(\mathrm{I})} = -0.5, \quad \Psi_2^{(\mathrm{I})} = -0.1, \tag{8.51}$$

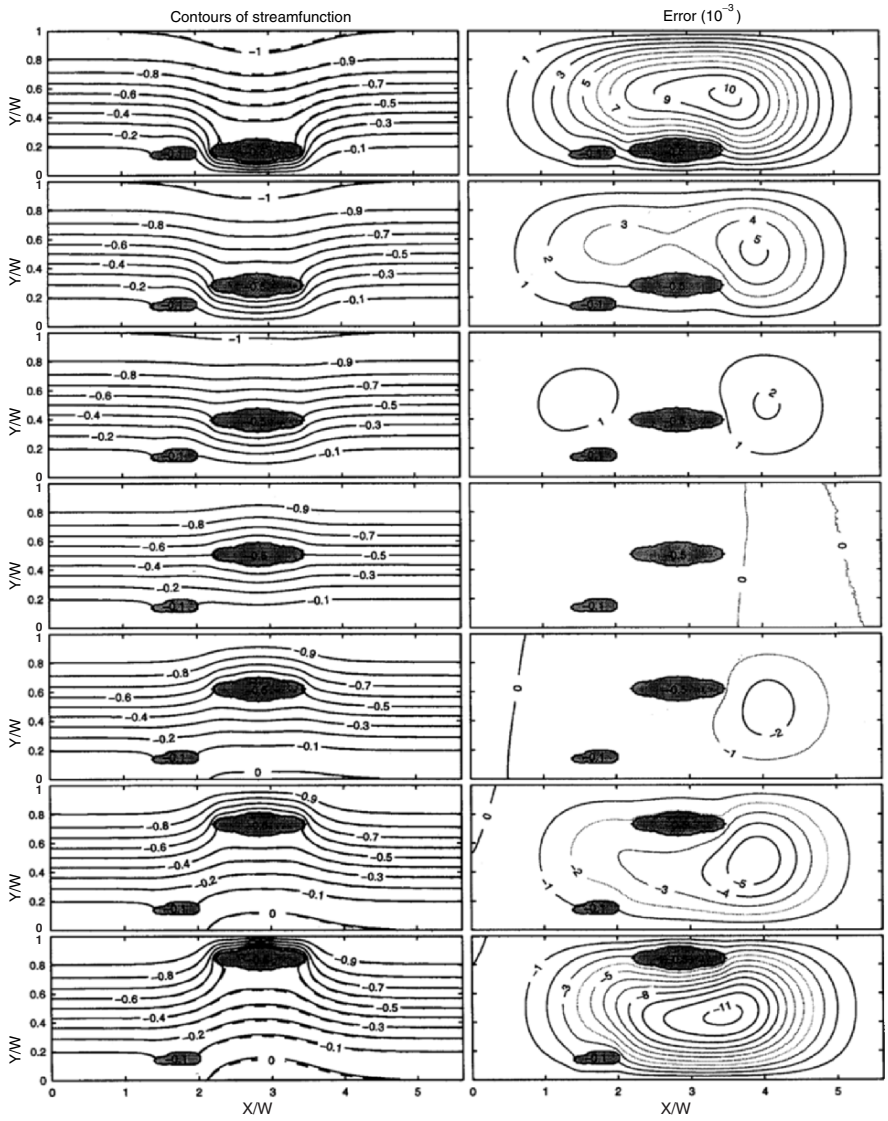

Fig. 8.11. *Left panels*: Comparison between $\Psi^{(\mathrm{ex})}(x, y)$ (*solid contours*) and $\Psi(x, y)$ (*dashed contours*) for varying location of Island-1 (keeping $\Psi_1^{(\mathrm{I})} = -0.5$) in the control run of the twin experiments. *Right panels*: The corresponding difference, $\Psi^{(\mathrm{ex})}(x, y) - \Psi(x, y)$, for each case

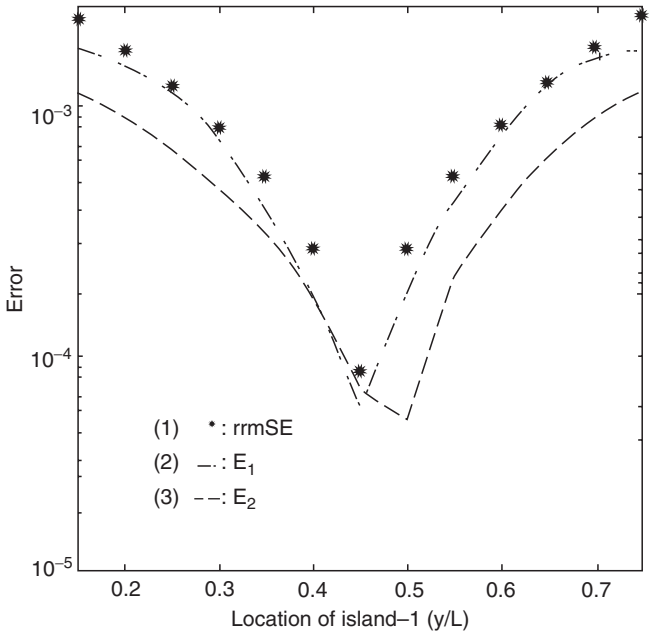

Fig. 8.12. Dependence of rrmse between $\Psi(x, y)$ and $\Psi^{(\mathrm{ex})}(x, y)$ over the whole channel (denoted by *asterisk*), and the relative errors E_1 (*dash-dotted*) and E_2 (*dashed*) on varying location of Island-1

and Island-1 located at the middle of the channel for the first experiment (shown in middle panels of Fig. 8.11). This "exact" solution has the minimum root mean square error in the twin experiments.

The solution $\Psi^{(\mathrm{ex})}(x, y)$ is also shown as the solid contours in Fig. 8.13. The corresponding results for the second experiment are shown as the dashed contours. As the noise level increases, the solution from the second experiment becomes noisy, but the flow pattern is quite stable. Figure 8.14 shows the rrmse between $\Psi(x, y)$ and $\Psi^{(\mathrm{ex})}(x, y)$ for the whole channel and the errors E_1 and E_2 for different noise levels. Generally, the rmse increases with the noise level from 1.6×10^{-3} (at the noise level of 0.0125) to 0.01 (at the noise level of 0.05). For the noise level of 0.05, the errors E_1 and E_2 are 0.053 and 0.02, respectively. This indicates that the use of this method to estimate the Ψ-values for islands will bring the error similar to (0.05 for Island-1's stream function) and less than (0.02 for Island-2's stream function) the noise level.

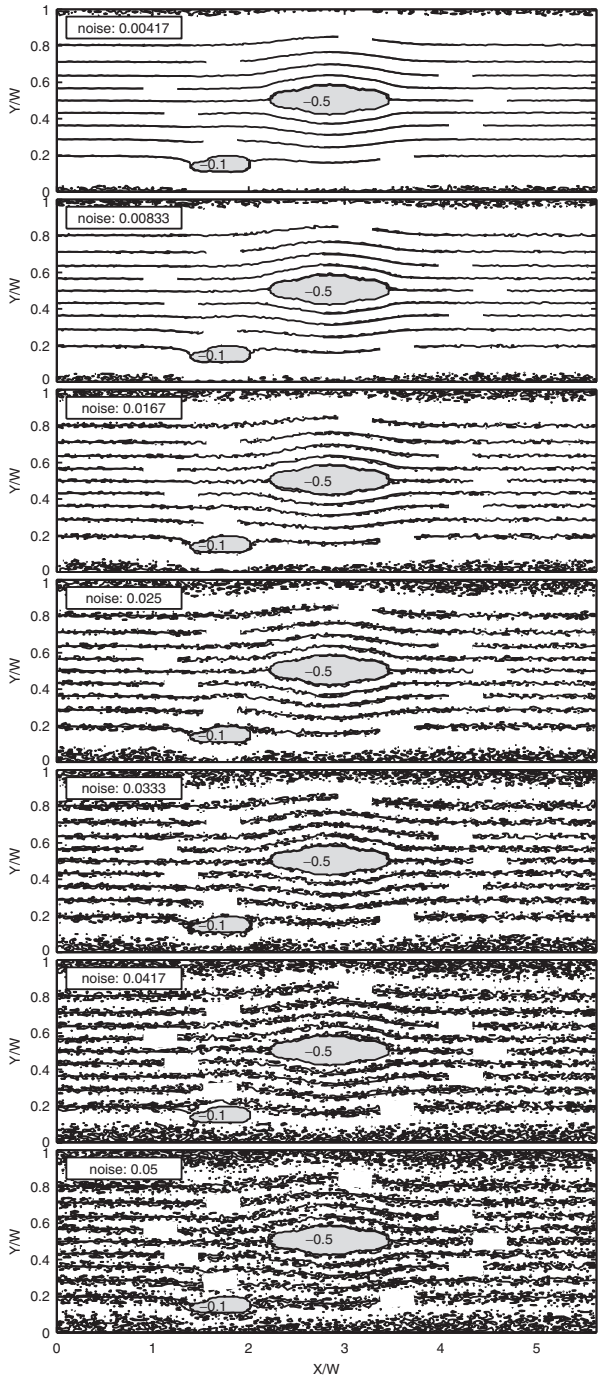

Fig. 8.13. Comparison between $\Psi^{(\mathrm{ex})}(x, y)$ (*solid contours*) and $\Psi(x, y)$ (*dashed contours*) for various noise levels from 0.00417 to 0.05

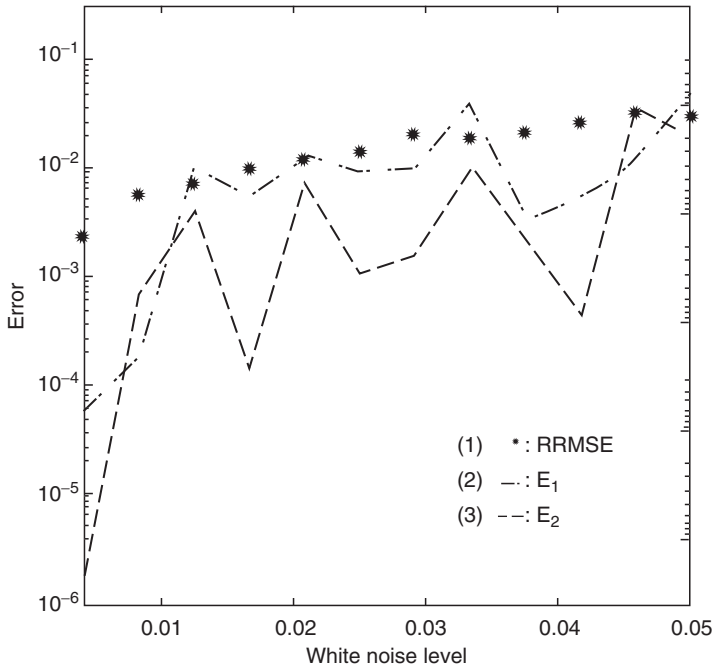

Fig. 8.14. Dependence of rrmse between $\Psi(x, y)$ and $\Psi^{(\mathrm{ex})}(x, y)$ over the whole channel (denoted by *asterisk*), and the relative errors E_1 (*dash-dotted*) and E_2 (*dashed*) on varying noise levels

8.7 Global Volume Transport Stream Function

8.7.1 Ψ-Values for Global Islands

The iteration method developed in Sect. 8.5 is used to determine Ψ-values at islands. Figure 8.15 shows the distribution of Ψ-values for each continent/island computed from the annual, January, and July mean hydrographic and wind data. Taking the annual mean as an example, we have: 0 Sv for the American Continent, 157.30 Sv for Antarctica, −21.74 Sv for Australia, −27.17 Sv for Madagascar, and −21.74 Sv for New Guinea.

8.7.2 Ψ-Values for Global Oceans

With the given values at the boundaries and islands, the Poisson Ψ-equation (8.18) is solved with the climatological annual and monthly Π-fields and obtain annual and monthly global Ψ-fields. After that, we use (8.17) to recompute the depth-integrated velocity $(\hat{U}, \hat{V})$. Since the NOAA WOA 1°×1° hydrographic (Levitus and Boyer 1994; Levitus et al. 1994) and wind data (da Silva et al. 1994) are used to compute Ψ-fields, small-scale topographic features

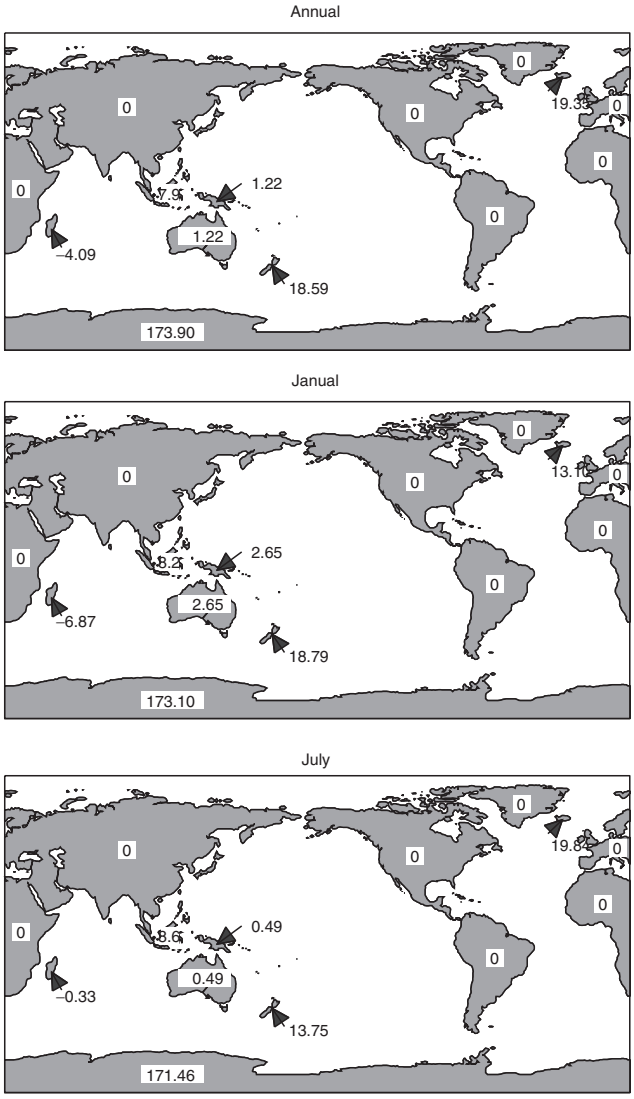

Fig. 8.15. Computed Ψ-values for each continent/island (**a**) annual mean, (**b**) January, and (**c**) July (from Chu and Fan 2006, Journal of Marine Systems)

such as English Channel, Taiwan Strait, Gilbralta Strait, and Bering Strait cannot be resolved. The global Ψ-field (Fig. 8.16) and depth-integrated velocity vector $(\hat{U}, \hat{V})$ field (Fig. 8.17) agree reasonably well with earlier studies (e.g., Reid 1989, 1994, 1997; Semtner and Chervin 1992) and show the capability of the P-vector method for determining main characteristics of global

circulation, such as the strong Antarctic Circumpolar Current, the well-defined subtropical and subpolar gyres, and the equatorial current system.

8.8 Sensitivity to Observational Errors

Usually, errors occur in hydrographic and wind data (observational errors) and in model discretization (i.e., computational errors). Sensitivity study is conducted on the solutions to the observational data errors before discussing the calculated circulation characteristics. Suppose the observational data errors have to be represented by a Gaussian-type random variable with a zero mean and a standard deviation of σ, then a random number generator (FORTRAN function, Ranf) is used to produce two sets of random noises for each grid point independently, with mean value of zero and standard deviation of σ (1) three-dimensional temperature error field with standard deviation of 0.2°C and (2) two-dimensional surface wind stress error field with standard deviation of $0.05\,\mathrm{N\ m^{-2}}$.

Stability of the inverse model is confirmed through the comparison between the annual mean Ψ-field with random errors in temperature data and surface wind stress data (Fig. 8.18b) and with the Ψ-field having no error added (Fig. 8.16). The inverse model has the capability to filter out noise in the forcing terms because of the major mathematical procedures of the model containing two integrations of the Poisson equation.

Questions and Exercises

(1) Derive the equations for the depth-integrated horizontal velocity

$$-f(\hat{V}-V) = A_z \left.\frac{\partial \hat{u}}{\partial z}\right|_{z=\eta} - A_z \left.\frac{\partial \hat{u}}{\partial z}\right|_{z=-H} + A_h \nabla_2^2 \hat{U}$$

$$-2A_h \nabla_2 u_{-H} \cdot \nabla_2 H - A_h u_{-H} \nabla_2^2 H, \tag{E8.1}$$

$$f(\hat{U}-U) = A_z \left.\frac{\partial \hat{v}}{\partial z}\right|_{z=\eta} - A_z \left.\frac{\partial \hat{v}}{\partial z}\right|_{z=-H} + A_h \nabla_2^2 \hat{V}$$

$$-2A_h \nabla_2 v_{-H} \cdot \nabla_2 H - A_h v_{-H} \nabla_2^2 H, \tag{E8.2}$$

from the basic (1.1a)–(1.1d).

(2) Discuss the physical significance of each term of the interim depth-integrated flow (U^*, V^*),

$$U^* = U_{\mathrm{den}} + U_{\mathrm{b}} + \frac{\tau_y}{f\rho_0}, \tag{E8.3}$$

$$V^* = V_{\mathrm{den}} + V_{\mathrm{b}} - \frac{\tau_x}{f\rho_0}. \tag{E8.4}$$

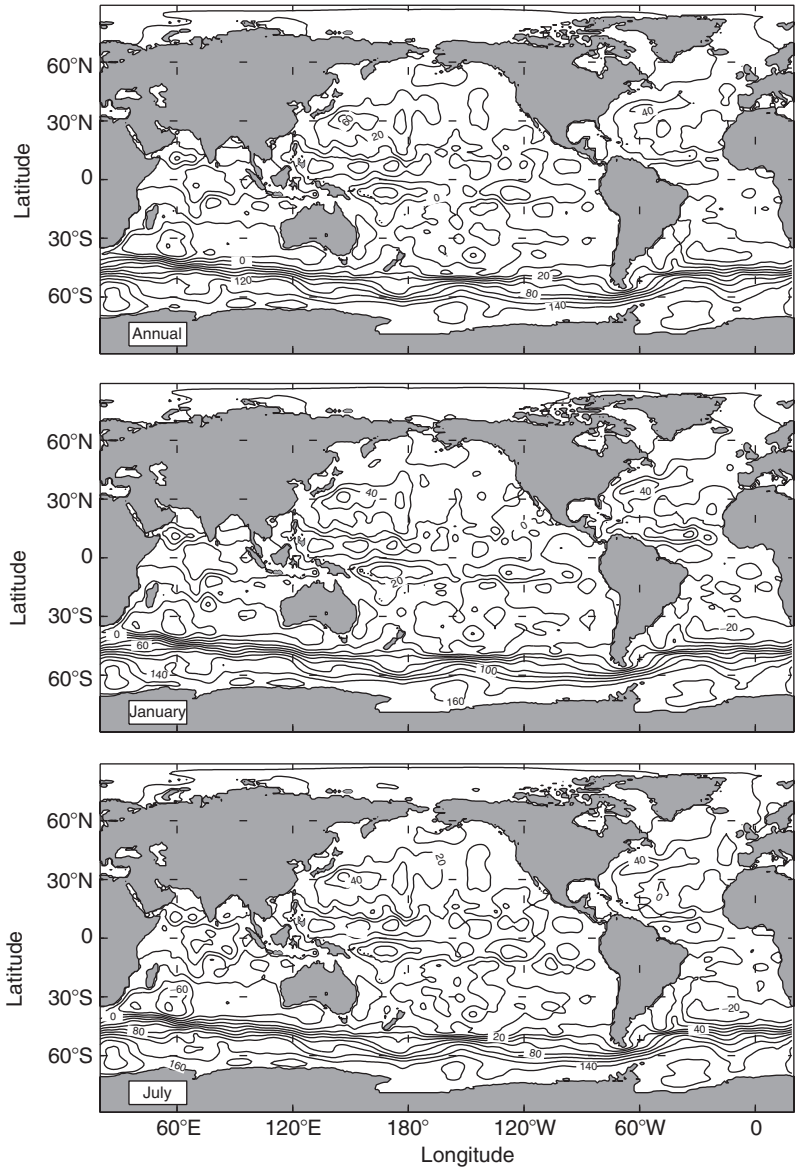

Fig. 8.16. Computed global volume transport stream function (Ψ) (**a**) annual mean, (**b**) January, and (**c**) July (from Chu and Fan 2006, Journal of Marine Systems)

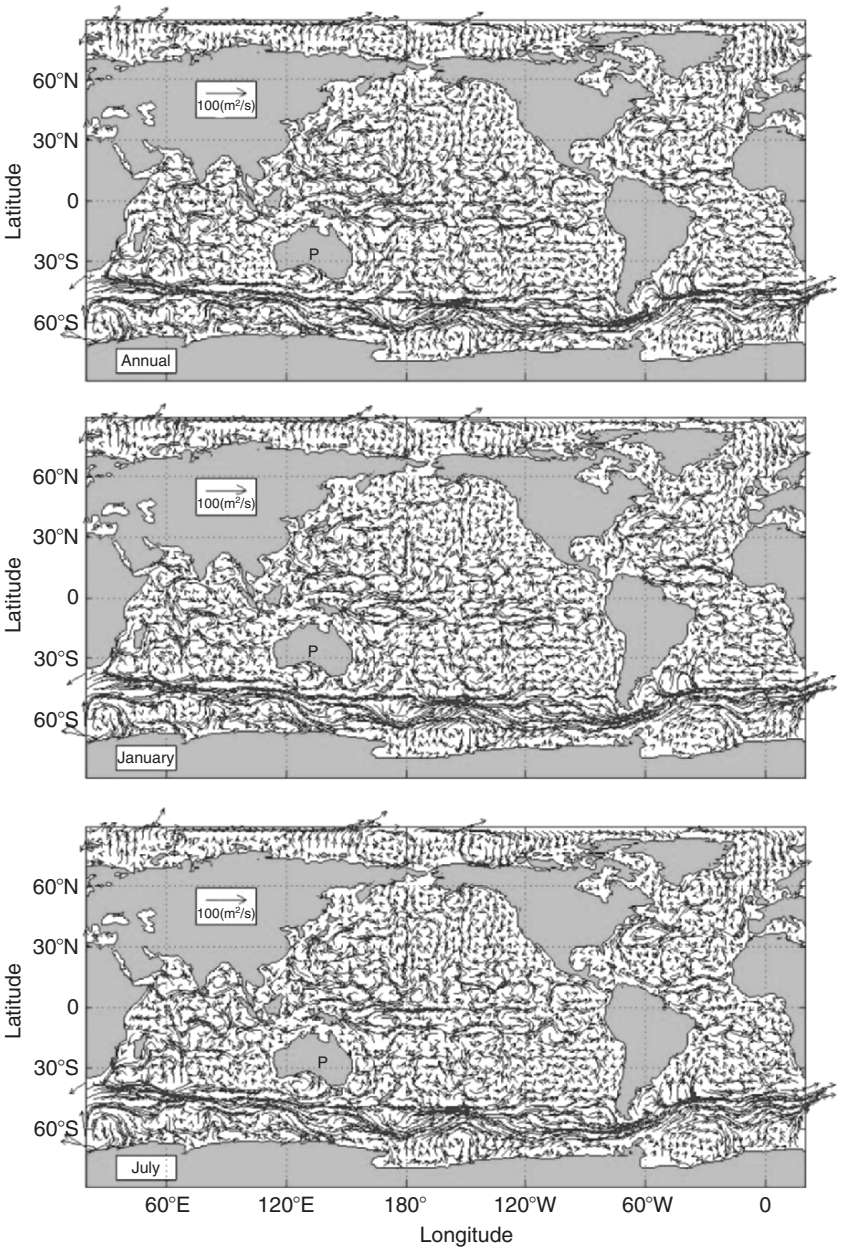

Fig. 8.17. Computed global depth-integrated velocity (U, V) vectors (**a**) annual mean, (**b**) January, and (**c**) July (from Chu and Fan 2006, Journal of Marine Systems)

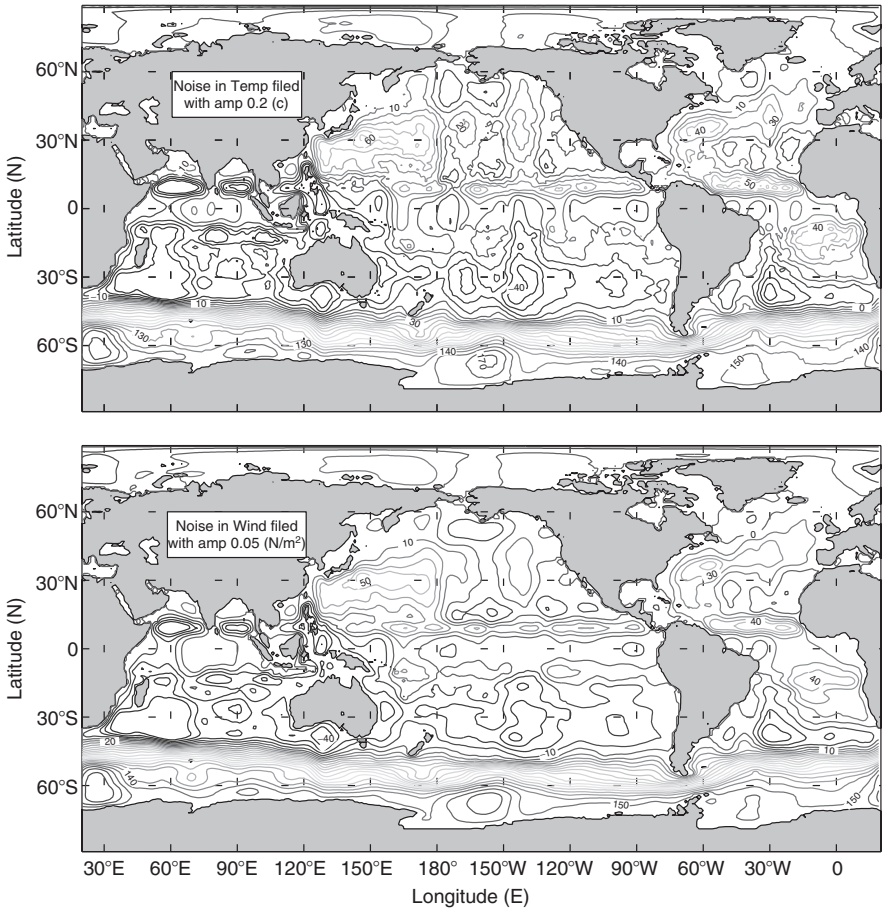

Fig. 8.18. Annual mean global volume transport stream function (Ψ) computed using the P-vector method with (**a**) three-dimensional Gaussian-type temperature errors (0-mean, 0.2°C-standard deviation) and (**b**) two-dimensional Gaussian-type surface wind stress errors (0-mean, $0.02\,\mathrm{N\,m^{-2}}$-standard deviation). The stochastic errors are introduced into all the gird points by random number generator

(3) Discuss the similarity and dissimilarity of the following equation

$$\nabla^2\Pi = \frac{\beta}{A_h}(\hat{V} - V_{\mathrm{den}} - V_{\mathrm{b}}) - \frac{1}{A_h\rho_0}\left(\frac{\partial\tau_y}{\partial x} - \frac{\partial\tau_x}{\partial y}\right) + \left(\frac{\partial Q_2}{\partial x} - \frac{\partial Q_1}{\partial y}\right), \tag{E8.5}$$

and the Munk equation.

(4) For a domain Ω with islands as $\Omega_j (j = 1, \ldots, N)$ shown in Fig. 8.5, prove that the volume transport stream function at Island-Ω_j can be computed approximately by

$$\Psi|_{\Omega_j} = \frac{\hat{\Gamma}_j - \Gamma_j^{(\mathrm{w})}}{A}, \tag{E8.6}$$

where $\Gamma_j^{(\mathrm{w})}$ is the circulation in the water and

$$A = -\sum_{l=1}^{N} \left(\frac{|J_{l+1} - J_l|\,\Delta y}{2\Delta x} + \frac{|I_{l+1} - I_l|\,\Delta x}{2\Delta y} \right),$$

$$\hat{\Gamma}_{j_j} = \frac{1}{2} \sum_{l=1}^{N} [\hat{\mathbf{V}}(I_{l,} J_l) + \hat{\mathbf{V}}(I_{l+1}, J_{l+1})]$$

$$\cdot[\mathbf{i}(I_{l+1} - I_l)\Delta x + \mathbf{j}(J_{L+1} - J_l)\Delta y].$$

(5) Search the literature and compare the Ψ-values of global islands identified using the Stokes Theorem and other methods.
(6) What are the major characteristics of the global circulation identified from the global volume transport stream function (Fig. 8.16) and depth-integrated horizontal velocity (Fig. 8.17)?
(7) Are the effects of noises in the temperature and wind observations large on the calculated annual mean global volume transport stream function form in comparison between Fig. 8.18 and Fig. 8.16a? Justify your answer.